Asian Journal of Chemistry; Vol. 35, No. 10 (2023), 2572-2578

ASIAN JOURNAL OF CHEMISTRY

https://doi.org/10.14233/ajchem.2023.28227

Photocatalytic Studies and Antibacterial Activity of Copper thiotungstate/ Reduced Graphine Oxide Nanocomposites (Cu_2WS_4/rGO)

PRIYA PERUMAL[1] and LAKSHMI MAHADEVAN[2,*]

[1]Department of Chemistry, Periyar University, Salem-636 011, India
[2]Department of Chemistry, Namakkal Kavignar Ramalingam Government Arts College for Women, Namakkal-637 001, India

*Corresponding author: E-mail: drmlakshmichemap@gmail.com

Received: 20 July 2023; *Accepted*: 21 September 2023; *Published online*: 28 September 2023; AJC-21412

A copper tungsten sulfide (Cu_2WS_4)-anchored reduced graphene oxide (Cu_2WS_4/rGO) nanocomposite was prepared using a feasible hydrothermal approach and succssfully employed as photocatalytic material for the degradation of reactive black-5 (RB-5) dye. In the preparation of Cu_2WS_4 and Cu_2WS_4/rGO nanocomposite, copper nitrate, tungsten oxalate, metallic sulfur, graphene oxide, sodium hydroxide and sodium borohydride were used as sources of precursors. The prepared materials (Cu_2WS_4 and Cu_2WS_4/rGO) were characterized by powder X-ray diffraction (PXRD), DRS-UV, FT-IR and Raman spectral analysis, whereas, the morphology and composition of Cu_2WS_4 and Cu_2WS_4/rGO were determined by TEM, FESEM and EDAX analyses. Under visible light conditions with a band gap of 1.8 eV, the degradation capacity of Cu_2WS_4/rGO nanocomposite towards reactive black-5 dye was enhanced and a dragadation efficiency of 98.2% was achieved at 120 min. The antimicrobial activity results of Cu_2WS_4/rGO nanocomposite showed that the prepared nanocomposites exhibit improved antibacterial activity 20% (*S. aureus*) and 10% (*P. aeruginosa*) growth inhibition

Keywords: Copper tungsten sulfide, Graphene Oxide, Hydrothermal synthesis, Reactive black-5, Antibacterial activity.

INTRODUCTION

The rapid growth of the global population has led to a substantial escalation in the consumption of various materials, such as cosmetics, electronics, *etc*. Consequently, there has been a corresponding rise in the generation of waste associated with these materials [1-3] and resulting the serious causes of water and soil pollution. Hence, the accelerating advancement of technology and a corresponding increase in consumer spending power are contributing to the proliferation of materials. Once they have reached their expiration date, these items may be deemed potentially harmful to both the environment and public health [4-6].

Transition metal chalcogenides are hugely important in today's concerns because of their exceptional qualities, including adjustable components, flexible structure, diverse shape, and distinctive electrical structure. These properties are used in various fields of applications like energy storage, electronic devices and catalysis [7-9]. Particularly, the transition metal chalcogenides are used to breakdown organic contaminants by photocatalysis [10-12]. Furthermore, in order to improve the cycle qualities and rate performance of chalcogenides, carbonaceous compounds like graphene have been employed by scientists [13-15] to enhance the cycle characteristics and rate performance of chalcogenides, as graphene possess enormous surface area, improved charge mobility, high thermal stability and mechanical strength. For example, CuS/rGO nanocomposites exhibit enhanced the photocatalytic performance compared with pure CuS [16].

The binary-layered transition metal chalcogenides anchored by reduced graphine oxide also show huge interest in dye degradation processes. For example, enhanced photocatalytic studies of the binary layered transition metal chalcogenides MoS_2 and TiS_2 are reported [17,18]. Similarly, Arumugam *et al.* [19] reported the NiS/rGO photocatalytic performance against methylene blue degradation under solar light irradiation whereas Dutta *et al*. [20] used hydrothermal synthesized ZnS/rGO for the degradation studies. Ternary transition metal chalcogenides also show better photocatalytic performance compared with binary-layered transition metal chalcogenides, for example.

This is an open access journal, and articles are distributed under the terms of the Attribution 4.0 International (CC BY 4.0) License. This license lets others distribute, remix, tweak, and build upon your work, even commercially, as long as they credit the author for the original creation. You must give appropriate credit, provide a link to the license, and indicate if changes were made.

Perera *et al*. [21] reported that $ZnMoS_4$ shows effective and selective cellular copper detoxifying agents. The ternary copper based metal chalcogenides likewise demonstrate better dye degradation activity [22-27].

Herein, a copper tungsten sulfide (Cu_2WS_4)-anchored reduced graphene oxide (Cu_2WS_4/rGO) nanocomposite was prepared by one-pot hydrothermal method. The introduction of copper nitrate, tungsten oxyalate, metallic sulfur and reduced graphene oxide significantly influences functional groups and their morphologies. Subsequently, the resulted Cu_2WS_4/rGO material displayed the tetragonal crystal structure, whereas Cu_2WS_4 has combined stable sheet-like morphologies. The higher Cu, W and S contents in rGO greatly modified the photocatalytic activity of the reactive black-5 dye degradation. Moreover, the antibacterial performance of synthesized Cu_2WS_4/rGO nanocomposite was also demonstrated by testing with *S. aureus* and *P. aeruginosa* bacterial strains.

EXPERIMENTAL

All of the chemical and reagents/solvents were purchased from Sigma-Aldrich and SRL (LR grade) and used without any purification.

Synthesis of pure Cu_2WS_4 and Cu_2WS_4 anchored rGO nanocomposite: The reduced graphene oxide was prepared by per reported [28] whereas Cu_2WS_4 was prepared by using hydrothermal method. In brief, 3 mM of copper nitrate was mixed in ethanol (30 mL) and the obtained solution was added dropwise to 3 mM of tungsten oxylate (Cu precursor) followed by the addition of 3 mM of sulfur solution under magnetic stirring for 2 h. Consequently, the obtained Cu_2WS_4 composite material was transferred into an autoclave and heated at 140 ºC for 8 h. Finally, the precipitate was filtered, washed with ethanol and dried.

In next step, the Cu_2WS_4/rGO nanocomposite was prepared by mixing 250 mg of prepared Cu_2WS_4 material with 30 mL of ethanol solution and continuously stirred for 2 h. Consequently, the above mixture was blended with 150 mg of rGO solution. Then the attained mixture was transferred to an autoclave and kept in a hot air oven at 140 ºC for 8 h. The obtained precipitate was washed several times with ethanol solvent.

Characterization: The purity of the sample's phase and structural aspects of Cu_2WS_4 and Cu_2WS_4/rGO were analyzed by an X-ray diffractometer (XRD) Rigaku with a scan rate of 3º/min and recorded a 2θ range of 10 to 90º. The morphologies of the sample Cu_2WS_4/rGO were examined by field emission scanning electron microscopy (FESEM) using ZEISS (EVO LS 15, Germany) instrument, whereas the elemental dispersive X-ray (EDX) analysis was performed with the help of AMETEK, Z2-17 analyzer (USA). Further, the insight morphologies and their crystalline nature analyses were also carried out by high resolution transmission electron microscopy (HRTEM, FEI). Fourier transform infrared spectra (Bruker Optic, Germany, TENSOR 27) were used to evaluate the bonding site of Cu_2WS_4/rGO materials.

Photocatalytic activity: The photocatalytic performance of the prepared materials, pure and nanocomposite, was evaluated by reactive black-5 dye solution (1mM) under a 500 W tungsten lamp providing visible light. In brief, 10 mg of catalyst was dispersed in 1 mL of dye solution and made up the volume to 100 mL of water. First, the beaker containing solution was stirred without any light sources, then the beaker containing solution was placed in the 500 W halogen lamp lights with an approximate distance of 15 cm. Also, two colling fans were fixed when the lights were on, and samples were collected after every 10 min and recorded for UV-Visible spectroscopy. Following this investigation, the photocatalyst was removed, The following equation was used to determine the effective percentage removal of dye as follows:

$$\text{Removal } (\%) = \frac{C_o - C}{C_o} \times 100$$

where C_o and C are the initial concentration and the concentration of the dye before and after degradation, respectively.

Langmuir-Hinshelwood kinetic model was carried out for the degradation analysis and can be represented as:

$$R = k\frac{KC}{1+KC}$$

where, R and C are the specific degradation reaction rate (mg/min) and the concentration of dye (mg), respectively. The k and K are the reaction rate constant (min) and the dye adsorption constant, respectively. Besides, the C is small, the above mentioned equation and obtained apparent pseudofirst-order equation is:

$$r = \frac{dC}{dt} = \frac{kKC}{1+KC}$$

$$-\ln\left(\frac{C}{C_o}\right) = k_{app}t$$

Antibacterial activity: The antibacterial activity of the material (Cu_2WS_4/rGO) was determined by disk diffusion method. The two microorganisms *i.e*. *Staphylococcus aureus* (Gram +ve) and *Pseudomonas aeruginosa* (Gram -ve) was used in this study. The antimicrobial activity was evaluated by measuring the diameter of inhibition zone. The Mueller-Hinton agar, with 0.5% (v/v) Tween-20 but no oil, was used as a growth control. Inoculated plates were incubated at 35 ºC for 48 h. Minimum inhibitory concentrations (MICs) were determined after 24 and 48 h. The assay was carried out in triplicates and control plates were also maintained.

RESULTS AND DISCUSSION

XRD studies: The synthesized Cu_2WS_4 and Cu_2WS_4/rGO nanocomposite with XRD patterns are demonstrated in Fig. 1. The observed XRD results showed peaks at 17.6º, 18.5º, 29.1º, 31.2º, 37.5º, 41.2º, 49.2º, 50.7º, 59.5º, 62.1º and 65.6º, which correspond to (002), (011), (112), (013), (022), (220), (024), (222), (125), (231) and (134) plane, respectively. The results are well matched with the standard pattern of Cu_2WS_4 materials (JCPDS no. 98-009-8909), indicating the tetragonal crystal system along with the space group of $I\bar{4}2m$. Notably, compared with Cu_2WS_4, the Cu_2WS_4/rGO nanocomposite

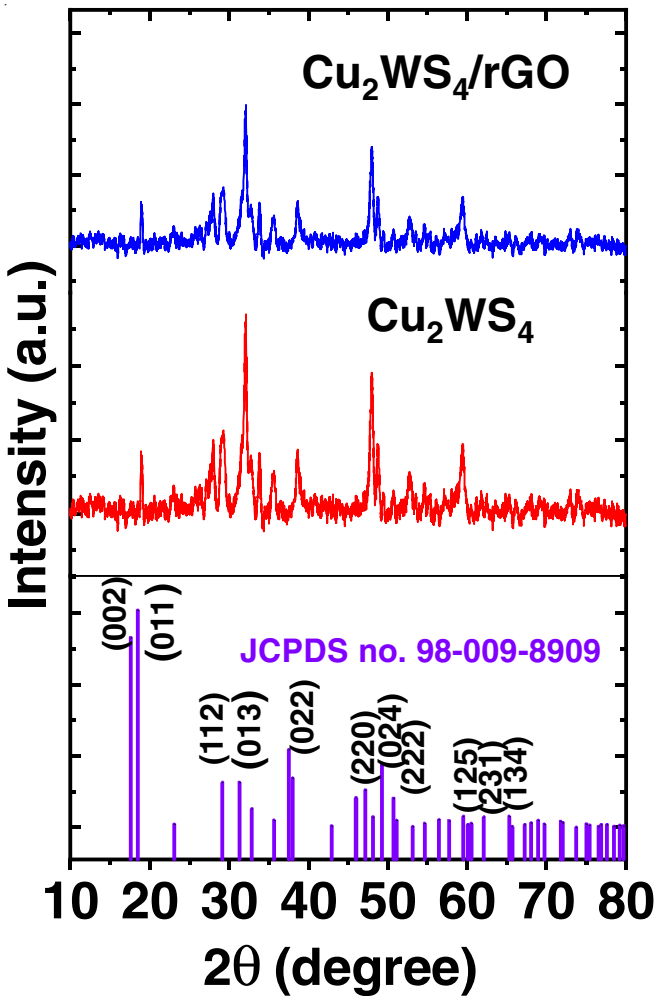

Fig. 1. Hydrothermally obtained sample of the XRD of Cu_2WS_4 and Cu_2WS_4/rGO

showed an altered intensity, which suggests the combination of rGO is greatly anchored over the Cu_2WS_4/rGO material.

FTIR studies: The FT-IR spectra of the prepared Cu_2WS_4 and Cu_2WS_4/rGO samples are shown in Fig. 2. The O-H stretching vibration has its distinctive peak in the pure Cu_2WS_4 sample at 2633 cm^{-1}. Additionally, the peaks at 2326, 2097 and 641 cm^{-1} correspond to the stretching vibrations of C=O, C-OH, and C-O-C, respectively [29]. The elimination of various oxygen functions greatly decreased the principal absorption peak intensities for the rGO sample, demonstrating that the hydrothermal procedure partially reduces GO [30]. The stretching and bending vibrations of the Cu-S and W-S bonds are represented by the peaks in the range of 1114-641 cm^{-1}, respectively. With small peak shifts to the low wavenumbers, the main characteristic peaks of rGO and Cu_2WS_4 were observed. These changes demonstrated that rGO and Cu_2WS_4 counterparts formed intimate interfacial contact. Additionally, the low concentration is to blame for the removal of the rGO peak in the Cu_2WS_4 nanocomposites.

Morphological studies: In Fig. 3(a-b), the morphology of the synthesized composite material is depicted as having a cauliflower-like shape, whereas Fig. 3(c-d) show the FE-SEM images of Cu_2WS_4 composites, which has a distinct structure

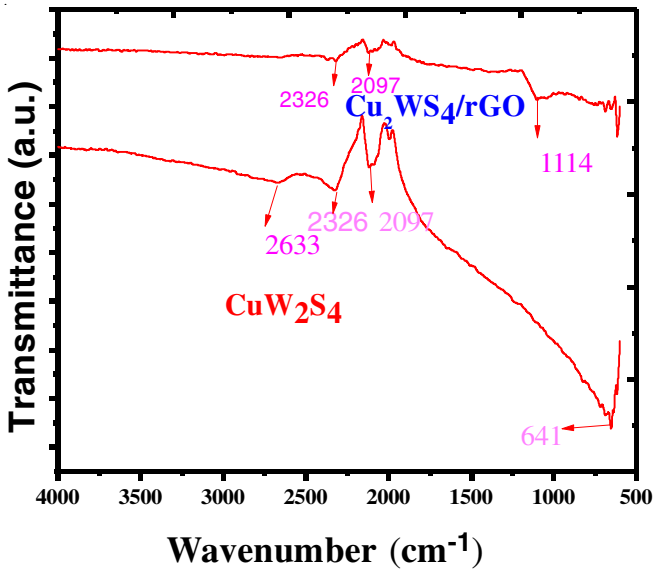

Fig. 2. FT-IR spectra of Cu_2WS_4 and Cu_2WS_4/rGO

from the composite material. The TEM images of the prepared Cu_2WS_4/rGO nanocomposite are shown in Fig. 4(a-c), which depicts the sheet-like structure. In Fig. 4d, the SAED pattern of Cu_2WS_4/rGO is shown with interplanar spacing of about 0.29 nm, which corresponds to the (113) lattices. The appearance of the homogenous structure indicates the existence of the strong interaction between the Cu_2WS_4 and rGO. The EDX mapping analysis was done to examine the elemental distribution in the Cu_2WS_4 nanocomposite. The elements Cu, W, S, O and C are uniformly distributed throughout the nanocomposite, according to the EDX data shown in Fig. 5a, further demonstrating the sample's purity.

Optical properties: The visible light range is well absorbed by both samples. Further evidence that rGO is not integrated into the crystal lattice of Cu_2WS_4 as provided by the composite sample's virtually identical absorption to that of pure Cu_2WS_4/rGO, which is compatible with the XRD studies [21]. The computed band gap energies for the Cu_2WS_4 and Cu_2WS_4/rGO nanocomposites, respectively, were 2.6 and 1.6 eV using Tauc's plots [22]. According to the UV-Vis DRS spectra (Fig. 6), the successful integration of rGO lowers the band gap and improves the nanocomposite's capacity to absorb visible light, which is advantageous for better photocatalytic activity.

Photocatalytic degradation studies: The reactive black-5 (RB-5) dye solutions containing catalysts were agitated in the dark for 30 min prior to being exposed to visible light in order to achieve the adsorption desorption equilibrium. The absence of photocatalyst in the aforementioned investigations demonstrated that the degradation of RB-5 dye did not occur during the light exposure, suggesting a limited occurrence of photolysis for RB-5 dye [28]. The Cu_2WS_4/rGO had increased photocatalytic activity in compared to pure Cu_2WS_4, as observed in Fig. 7a.

The pseudo-first-order kinetics of RB-5 dye photodegradation using Cu_2WS_4/rGO nanocomposites is well described by the equation: $\ln(C/C_o) = -kt$, where C_o is the initial concentration of dye; C represents the concentration of dye at given

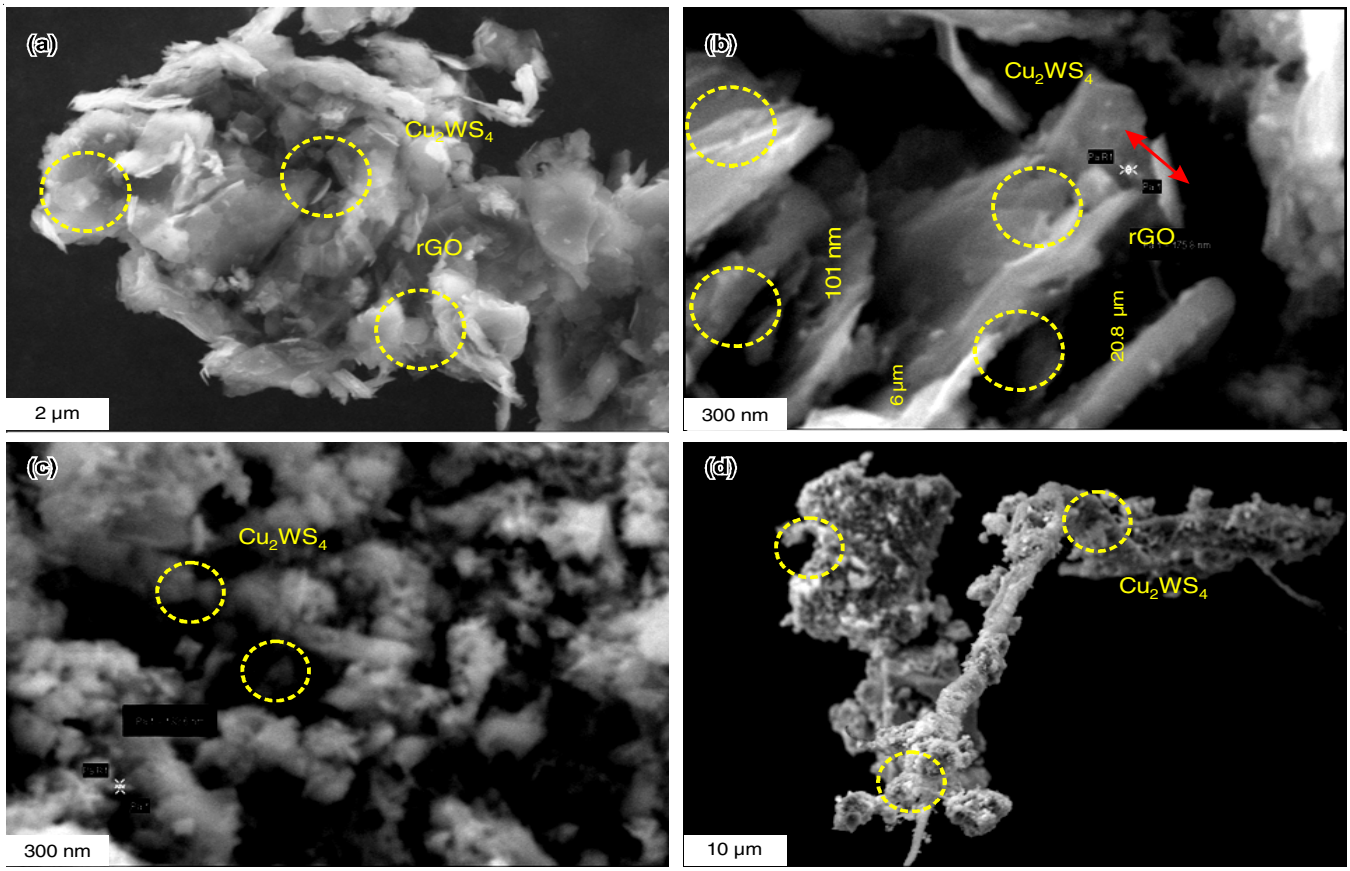

Fig. 3. SEM images of (a,b) Cu_2WS_4/rGO and (c,d) Cu_2WS_4

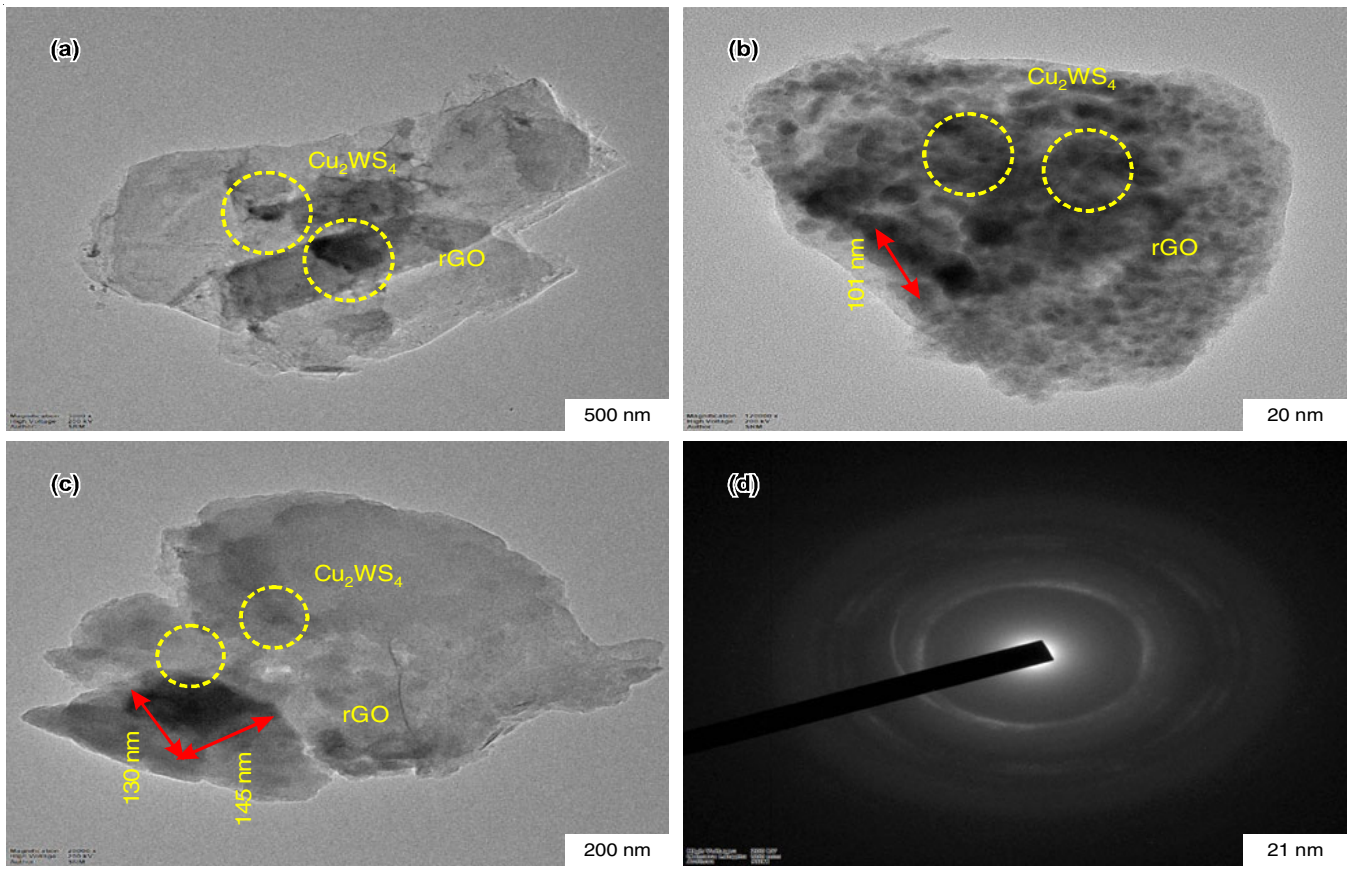

Fig. 4. TEM images of (a,b,c) Cu_2WS_4/rGO and (d) Cu_2WS_4/rGO

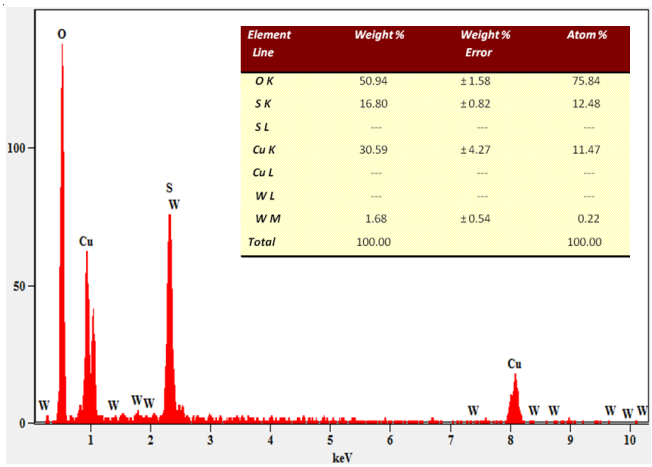

Fig. 5. EDX images of the Cu_2WS_4

time intervals t; and k is the pseudo-first-order rate constant [22]. The aspect of reusability holds significant importance in the practical application of photocatalysts. Thus, in order to assess the stability of the prepared Cu_2WS_4/rGO photocatalyst, the recycling experiments (n = 4) were performed under the identical conditions. As can be seen in Fig. 7b, the photocatalyst activity decreases by roughly 22% after five cycles of exposure to visible light.

Photocatalytic mechanism: The findings obtained from the DRS UV-Vis analysis, along with previous reports, have contributed to the proposal of a potential mechanism. The following equations were used to determine the Cu_2WS_4/rGO valence band (VB) and conduction band (CB) edge potentials [22,31].

$$E_{VB} = \chi - E_e + 0.5E_g$$

$$E_{CB} = E_{VB} - E_g$$

where χ is the free electron energy of the hydrogen scale (4.5 eV), E_g is the band gap energy of the semiconductor (2.6 eV for Cu_2WS_4). As a result, the VB and CB potentials of Cu_2WS_4 material were determined to be 2.6 eV (E_{VB}) and -1.13 eV (E_{CB}), respectively [19]. Thus, Cu_2WS_4 is a material that can be stimu-

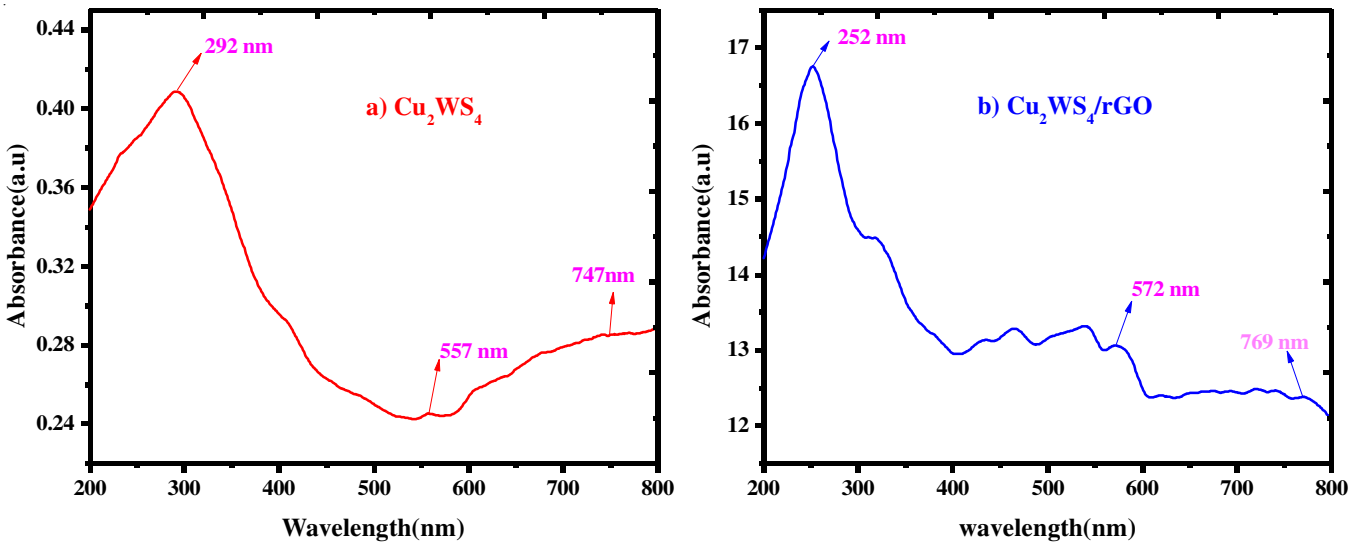

Fig. 6. DRS UV-vis spectrum of (a) Cu_2WS_4 and (b) Cu_2WS_4/rGO

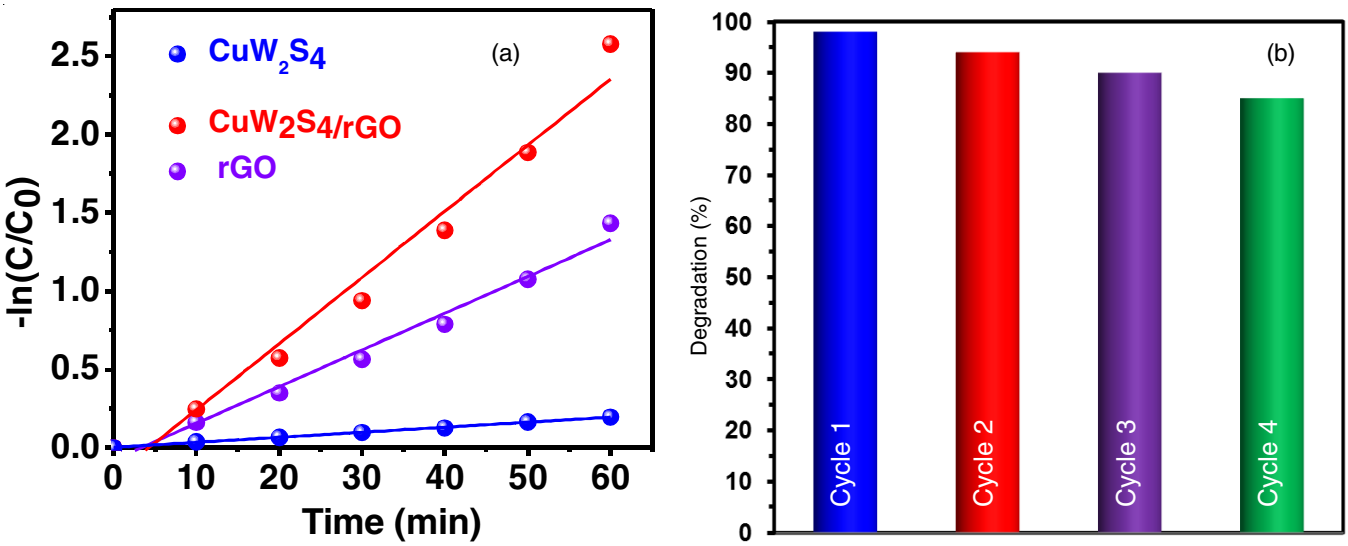

Fig. 7. Degradation spectrum of (a) Cu_2WS_4/rGO and (b) reusability of the Cu_2WS_4/rGO

lated to produce electrons and holes when exposed to visible light. In Cu_2WS_4/rGO nanocomposite, the RGO can function as an efficient electron transfer medium, resulting in the effective charge separation and increasing the activity of photocatalyst [22]. As a result, the Cu_2WS_4 nanocomposites with rGO incorporation exhibit greater photocatalytic activity toward the reactive black-5 (RB-5) dye degradation.

Antibacterial activity: The antibacterial activity of the material is proportional to the particle size, with higher activity being displayed by smaller particles due to their greater surface area. Fig. 8(a-b) displays the lack of antibacterial action of Cu_2WS_4/rGO against *Staphylococcus aureus* and *Pseudomonas aeruginosa* after 12 h. However, the antibacterial activity was detected in the same material under the same condition after 48 h of treatment (Fig. 8c-d). Thus, these bacteria are susceptible to the antibacterial properties of the prepared Cu_2WS_4/rGO material.

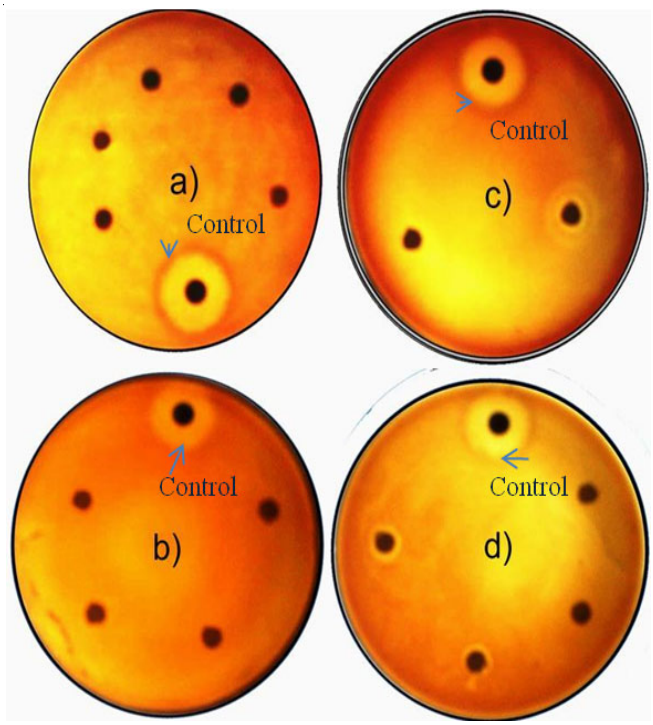

Fig. 8. (a,b) Antimicrobial activity of the *Staphylococcus aureus* and *Pseudomonas aeruginosa* for Cu_2WS_4/rGO at 12 h there is no activity present. The same material at same condition treated with 48 h the materials showed some degree of antibacterial activity found (c,d). Resulting that the materials Cu_2WS_4/rGO shows antibacterial activity against the investigated bacterial strain

Conclusion

In this study, the hydrothermal synthesis of Cu_2WS_4 and Cu_2WS_4/rGO nanocomposite was achieved. SEM and TEM analyses confirmed that the Cu_2WS_4 nanocomposite were uniformly and effectively adhered to the rGO sheets. The Cu_2WS_4/rGO nanocomposites demonstrated excellent photocatalytic degradation toward the degradation of the reactive black-5 (RB-5) dye when exposed to the visible light. The prepared Cu_2WS_4/rGO nanocomposite also showed the promising results in the antibacterial investigations.

CONFLICT OF INTEREST

The authors declare that there is no conflict of interests regarding the publication of this article.

REFERENCES

1. V. Duraisamy, V. Sudha, V. Dharuman and S.M. Senthil Kumar, *ACS Biomater. Sci. Eng.*, **9**, 1682 (2023); https://doi.org/10.1021/acsbiomaterials.2c01248
2. V. Duraisamy, N. Arumugam, A.I. Almansour, Y. Wang, T.X. Liu and S.M.S. Kumar, *Colloids Surf. A Physicochem. Eng. Asp.*, **656**, 130347 (2023); https://doi.org/10.1016/j.colsurfa.2022.130347
3. M. Mahanthappa, V. Duraisamy, P. Arumugam and S.M. Senthil Kumar, *ACS Appl. Nano Mater.*, **5**, 18417 (2022); https://doi.org/10.1021/acsanm.2c04170
4. M.P. Kusturic, M. Jevtic and J.T. Ristovski, *Front. Environ. Sci.*, **10**, 1077974 (2022); https://doi.org/10.3389/fenvs.2022.1077974
5. D.P. Mohapatra, S.K. Brar, R.D. Tyagi and R.Y. Surampalli, *Chemosphere*, **78**, 923 (2010); https://doi.org/10.1016/j.chemosphere.2009.12.053
6. S.H. Kim, S. Chun, J.Y. Jang, H.D. Chae, C.-H. Kim and B.M. Kang, *Fertil Steril.*, **95**, 357 (2011); https://doi.org/10.1016/j.fertnstert.2010.07.1059
7. M. Saranya and A. Nirmala Grace, *J. Nano Res.*, **18-19**, 43 (2012); https://doi.org/10.4028/www.scientific.net/JNanoR.18-19.43
8. A. Shawky, S.M. El-Sheikh, A. Gaber, S.I. El-Hout, I.M. El-Sherbiny and A.I. Ahmed, *Appl. Nanosci.*, **10**, 2153 (2020); https://doi.org/10.1007/s13204-020-01283-4
9. K. Krishnamoorthy, G. Kumar Veerasubramani, A.N. Rao and S. Jae Kim, *Mater. Res. Express*, **1**, 035006 (2014); https://doi.org/10.1088/2053-1591/1/3/035006
10. P.O. Fadojutimi, S.S. Gqoba, Z.N. Tetana and J. Moma, *Catalysts*, **12**, 468 (2002); https://doi.org/10.3390/catal12050468
11. E.C. Okpara, O.C. Olatunde, O.B. Wojuola and D.C. Onwudiwe, Environ. Adv., 11, 100341 (2023). https://doi.org/10.1016/j.envadv.2023.100341
12. L. Nie and Q. Zhang, *Inorg. Chem. Front.*, 4, 1953 (2017); https://doi.org/10.1039/C7QI00651A
13. K. Mensah-Darkwa, D.N. Ampong, E. Agyekum, F.M. de Souza and R.K. Gupta, *Energies*, **15**, 4052 (2022); https://doi.org/10.3390/en15114052
14. A. Mondal, A. Prabhakaran, S. Gupta and V.R. Subramanian, *ACS Omega*, **6**, 8734 (2021); https://doi.org/10.1021/acsomega.0c06045
15. R.A. El-Gendy, H.M. El-Bery, M. Farrag and D.M. Fouad, *Sci. Rep.*, **13**, 7994 (2023); https://doi.org/10.1038/s41598-023-34743-2
16. J. Shi, X. Zhou, Y. Liu, Q. Su, J. Zhang and G. Du, *Mater. Lett.*, **126**, 220 (2014); https://doi.org/10.1016/j.matlet.2014.04.051
17. Y. Li, H. Wang, L. Xie, Y. Liang, G. Hong and H. Dai, *J. Am. Chem. Soc.*, **133**, 7296 (2011); https://doi.org/10.1021/ja201269b
18. J. Jeon, J.W. Jeong and Y.S. Jung, *Electron. Mater. Lett.*, **15**, 613 (2019); https://doi.org/10.1007/s13391-019-00153-8
19. P. Arumugam, P. Sengodan, N. Duraisamy, R. Rajendran and V. Vasudevan, *Ionics*, **26**, 4201 (2020); https://doi.org/10.1007/s11581-020-03564-y
20. S. Dutta, S. Chatterjee, I. Mukherjee, R. Saha and B.P. Singh, *Ind. Eng. Chem. Res.*, **56**, 4768 (2017); https://doi.org/10.1021/acs.iecr.7b00107
21. V.S. Perera, N.P. Wickramaratne, M. Jaroniec and S.D. Huang, *J. Mater. Chem. B Mater. Biol. Med.*, **2**, 257 (2014); https://doi.org/10.1039/C3TB20962H
22. W.C. Liu, B.L. Guo, X.S. Wu, F.M. Zhang, C.L. Mak and K.H. Wong, *J. Mater. Chem. A Mater. Energy Sustain.*, **1**, 3182 (2013); https://doi.org/10.1039/c3ta00357d

23. S. Vadivel, B. Paul, A. Habibi-Yangjeh, D. Maruthamani, M. Kumaravel and T. Maiyalagan, *J. Phys. Chem. Solids*, **123**, 242 (2018); https://doi.org/10.1016/j.jpcs.2018.08.011
24. S. Yao, L. Xu, Q. Gao, X. Wang, N. Kong, W. Li, J. Wang, G. Li and X. Pu, *J. Alloys Compd.*, **704**, 469 (2017); https://doi.org/10.1016/j.jallcom.2017.02.069
25. J. Wu, J. He, F. Li and X. Hu, *Catal. Lett.*, **147**, 215 (2017); https://doi.org/10.1007/s10562-016-1907-2
26. Q. Jia, Y.C. Zhang, J. Li, Y. Chen and B. Xu, *Mater. Lett.*, **117**, 24 (2014); https://doi.org/10.1016/j.matlet.2013.11.110
27. R. Rameshbabu, R. Vinoth, M. Navaneethan, S. Harish, Y. Hayakawa and B. Neppolian, *Appl. Surf. Sci.*, **418**, 128 (2017); https://doi.org/10.1016/j.apsusc.2017.02.126
28. G. Gnanamoorthy, P. Priya, D. Ali, M. Lakshmi, V.K. Yadav and R. Varghese, *Chem. Phys. Lett.*, **781**, 139011 (2021); https://doi.org/10.1016/j.cplett.2021.139011
29. M. Yildirim, F. Özel, A. Sarilmaz, A. Aljabour and I.H. Patir, *J. Mater. Sci. Mater. Electron.*, **28**, 6712 (2017); https://doi.org/10.1007/s10854-017-6365-0
30. I.H. Patir, E. Aslan, G. Yanalak, M. Karaman, A. Sarilmaz, M. Can, M. Can and F. Ozel, *Int. J. Hydrogen Energy*, **44**, 1441 (2019); https://doi.org/10.1016/j.ijhydene.2018.11.161
31. Z. Lei, W. You, M. Liu, G. Zhou, T. Takata, M. Hara, K. Domen and C. Li, *Chem. Commun.*, **3**, 2142 (2003); https://doi.org/10.1039/b306813g